



# The evolution of vortices determines the aeroacoustics generated by a hovering wing

Xueyu Ji<sup>1,‡</sup>, Bruce Ruishu Jin<sup>1</sup>, Qiuxiang Huang<sup>1,§</sup>, Li Wang<sup>1</sup>, Sridhar Ravi<sup>1</sup>, John Young<sup>1</sup>, Joseph C.S. Lai<sup>1</sup> and Fang-Bao Tian<sup>1,†</sup>

<sup>1</sup>School of Engineering and Technology, University of New South Wales, Canberra, ACT 2600, Australia

(Received 21 February 2024; revised 8 September 2024; accepted 2 November 2024)

The effects of the evolution of vortices on the aeroacoustics generated by a hovering wing are numerically investigated by using a hybrid method of an immersed boundary–finite difference method for the three-dimensional incompressible flows and a simplified model based on the Ffowcs Williams-Hawkings acoustic analogy. A low-aspect-ratio ( $AR = 1.5$ ) rectangular wing at low Reynolds ( $Re = 1000$ ) and Mach ( $M = 0.04$ ) numbers is investigated. Based on the simplified model, the far-field acoustics is shown to be dominated by the time derivative of the pressure on the wing surface. Results show that vortical structure evolution in the flow fields, which is described by the divergence of the convection term of the incompressible Navier–Stokes equations in a body-fixed reference frame, determines the time derivative of the surface pressure and effectively the far-field acoustics. It dominates over the centrifugal acceleration and Coriolis acceleration terms in determining the time derivative of the surface pressure. The position of the vortex is also found to affect the time derivative of the surface pressure. A scaling analysis reveals that the vortex acoustic source is scaled with the cube of the flapping frequency.

**Key words:** swimming/flying, aeroacoustics

## 1. Introduction

The aeroacoustics generated by flapping wings is ubiquitous in aerial animal flight. Wing-flapping-generated sound (Clark 2021) is essential in courtship (Spieth 1974; Gibson & Russell 2006) and sexual recognition (Warren, Gibson & Russell 2009) for many insects. Some insects, such as *Drosophila melanogaster*, can respond to sounds that share similar frequency characteristics to their own species (Robert & Göpfert 2002).

† Email address for correspondence: [fangbao.tian@unsw.edu.au](mailto:fangbao.tian@unsw.edu.au)

‡ Current address: Queensland Micro and Nanotechnology Centre, Griffith University, Nathan Campus, QLD 4111, Australia.

§ Current address: School of Mechanical, Medical and Process Engineering, Queensland University of Technology, George St, Brisbane City, QLD 4000, Australia.

Apart from biological systems, aeroacoustics generated by flapping wings is of importance in micro aerial vehicles (MAVs), especially in applications like military reconnaissance and environmental monitoring where quiet operation is crucial, because applications of flapping wings (Platzer *et al.* 2008; Shyy *et al.* 2010; Ravi *et al.* 2016) in the MAVs (Young & Garratt 2020; Chen *et al.* 2024) have been growing due to their high-lift performance.

In order to explain the aeroacoustics generated by flapping wings, it is necessary to introduce their force generation and the associated mechanisms, of which the majority are about the vortical structures. Early efforts on flapping wings were focused on their force generation (Ellington 1984; Platzer *et al.* 2008; Shyy *et al.* 2010). In particular, the influences of parameters (such as kinematics, aspect ratio and Reynolds numbers) on forces have been investigated. The kinematics of simplified flapping motions on the force generation have been extensively studied, including plunging and pitching motions in forward flight (Lai & Platzer 1999; Young & Lai 2007; Visbal 2009; Kim & Gharib 2010), and translating/stroke and pitching motions in hovering flight (Birch & Dickinson 2001; Poelma, Dickson & Dickinson 2006; Garmann, Visbal & Orkwis 2013; Medina & Jones 2016). It is found that unsteady flows over the flapping wing generate vortices near the wing edges which play an important role in the force generation in addition to the added mass (Chang 1992; Sane & Dickinson 2001). These vortical structures are demonstrated in figure 1, including leading-edge vortex (LEV) (Ellington *et al.* 1996; Ford & Babinsky 2013; Eldredge & Jones 2019), trailing-edge vortex (TEV) (Shyy *et al.* 2010; Han *et al.* 2015), tip vortex (TV) (Ringuette, Milano & Gharib 2007; Shyy *et al.* 2009; Kim & Gharib 2010), root vortex (RV) (Shyy *et al.* 2010) and sometimes secondary vortex (SV) (Lu, Shen & Lai 2006). The LEV is the most prominent flow structure. It creates a low-pressure zone above the wing, responsible for most of the lift generation during the translation/middle stroke phase (Ellington *et al.* 1996; Liu *et al.* 1998). Garmann & Visbal (2014) found that the aerodynamic force coefficients of revolving wings are hardly changed when the aspect ratio is larger than 2, as the chordwise evolution of LEV at outboard region is limited by the trailing edge, leading to the loss of the negative pressure above the wing. Jones & Babinsky (2011) investigated a waving wing at different Reynolds numbers, finding that the LEV sheds earlier at lower Reynolds numbers, leading to the earlier disappearance of the low-pressure zone and consequently a reduction of the aerodynamic forces. Other vortices contribute to the force in a similar way, i.e. through creating a low-pressure zone. Their contributions to the force are affected by shapes, kinematics and material properties of the wing (see e.g. Tian *et al.* 2013; Shahzad *et al.* 2016; Huang *et al.* 2023). Therefore, their evolution and interaction are quite diverse, creating complexities in studying flapping wings. For example, the interaction between LEV and the boundary layer could generate an SV which influences the force generation (Lu *et al.* 2006). Overall, the variations of these parameters will lead to the change of the vortex dynamics around the flapping wing, and thus modify the aerodynamic forces which could ultimately affect the aeroacoustics generated by the wings.

Conservation of momentum and force partition methods can be used to uncover the relationship between the vorticity and forces (Wu, Ma & Zhou 2007). Wu (1981) proposed the vorticity moment theory based on the conservation of momentum, connecting the aerodynamic force of a body moving in a fluid to the time derivative of the total first moment of the vorticity field in an open space. Based on a derivative of moment transformations, Wu, Pan & Lu (2005) further proposed two formulae to account for the aerodynamic forces on an arbitrary body in the form of control surface integral including the viscous vortical effects. This method was later successfully adopted by Li & Lu (2012) to calculate the aerodynamic forces of flapping plates by considering the ring-like vortical structures in the wake, finding that the force on a flapping plate is dominated by the flow

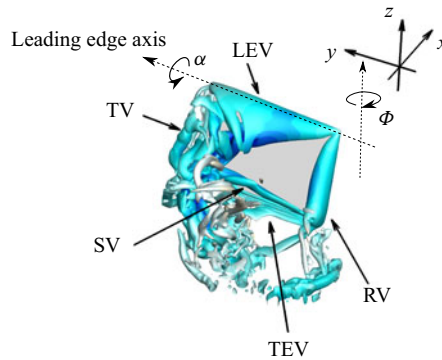


Figure 1. Vortical structures around a flapping wing: LEV, TEV, TV, RV and SV.

structures close to the plate. A force and moment partitioning method is a powerful tool for analysing complex vortex flows through delineating the contribution of vortex-induced effects (Wu *et al.* 2007; Menon, Kumar & Mittal 2022). For example, Seo, Menon & Mittal (2022) proposed a force partitioning method for studying the vortex evolution on the surface pressure fluctuation and acoustics of a two-dimensional (2-D) flapping foil. Further discussion on the relationship between vortices and aerodynamic forces can be found in Wu, Liu & Liu (2018). As the vortex flows dominate in flapping wings, their forces can be estimated by considering the time derivative of the vortex impulse, which is the basis of scaling laws for the aerodynamic forces of flapping wings (see e.g. Dewey *et al.* 2013; Kang & Shyy 2013; Lee, Choi & Kim 2015; Ehrenstein 2019; Liu, Liu & Huang 2022). In these scaling laws, the flapping frequency with its intrinsic connection with vortices' evolution period is considered as an important factor for scaling the aerodynamic forces.

The aerodynamic forces acting on a moving body, which are determined by the vortex flows, have strong effects on the acoustics (Seo, Hedrick & Mittal 2019; Tian 2020). Therefore, the vortical flows as well as their evolution would have a strong impact on the acoustics. However, the aeroacoustic characteristics have received less attention compared with the aerodynamics and vortical flows of flapping wings but have attracted growing effort recently. The aeroacoustics of flapping wings have been investigated experimentally (see e.g. Sueur, Tuck & Robert 2005; Arthur *et al.* 2014; Zhou *et al.* 2019) and numerically (see e.g. Nagarajan & Lele 2005; Nagarajan, Hahn & Lele 2006; Bae & Moon 2008; Inada *et al.* 2009; Wang & Tian 2020). The noise generated by a flyer in forward and aft directions is dominated by the first harmonic (flapping frequency,  $f_0$ ) while the noise at the sides is dominated by the second harmonic ( $2f_0$ ) (Sueur *et al.* 2005; Arthur *et al.* 2014). This is because that the wing creates one-periodic thrust in the forward and aft directions, and two-cycle lateral forces in side directions during one flapping cycle. Vorticity features also have an impact on acoustics. For example, the vortex shedding frequency near the trailing edge of a pitching NACA0012 aerofoil at high Reynolds numbers corresponds to the central frequency of the noise hump in the spectrum (Zhou *et al.* 2019). For a 2-D elliptical wing undergoing hovering and forward flights, a dipole source of flapping frequency is generated from the transverse motion and higher-frequency dipole sources arise from trailing edge scattering during tangential motion (Bae & Moon 2008). The dipole sources are generated by the pressure difference between the two sides of the wings (Inada *et al.* 2009). A more detailed study (Seo *et al.* 2019) showed that the time derivative of the surface pressure is the most important noise source for the aeroacoustics of flapping

wings at low Mach numbers (also see Tian 2020; Clark 2021). Flexibility of wings could enhance the mean force production and reduce the noise (Geng *et al.* 2017).

As noted above, the aerodynamic force fluctuations are correlated with the surface pressure variation caused by vortical structure evolution, hence new insights into the mechanism of aeroacoustics generation could be obtained by investigating the vortical structure evolution. Nedunchezian, Kang & Aono (2019) found that the kinematics of the wing play an important role in determining the noise level and that the variations of the vortical structures' topology may account for the difference in noise level. Clark (2021) discussed the vortex–wing interaction and acknowledged that the noise generated by vortices can be promoted if the vortices are in the vicinity of a wing (also noted by Curle (1955)). By using a force partitioning method, Seo *et al.* (2022) investigated the influences of each vortical structure and kinematic parameters on the aeroacoustics of a 2-D pitching NACA0015 aerofoil finding that the LEV plays an important role in determining the wing surface pressure and thus the far-field acoustics. However, the influence of characteristic vortices on surface pressure fluctuations in the three-dimensional (3-D) case can be evaluated in a more straightforward way without employing the projection method (Seo *et al.* 2022). In addition, it remains unclear which characteristic vortex is dominant in affecting the surface pressure fluctuations in the 3-D case.

To gain insights into the flow and acoustic fields associated with flapping wings, computational fluid dynamics (CFD) is an attractive method. There are two types of CFD methods used for aeroacoustic studies: (i) direct numerical simulation (DNS) and (ii) hybrid methods. In DNS, the compressible Navier–Stokes (NS) equations are solved by high-resolution numerical schemes in which all fluid scales and sound waves are resolved (Colonius, Lele & Moin 1997; Sandberg *et al.* 2009). Direct numerical simulation has been successfully used to investigate the aeroacoustics of flapping wings (Wang & Tian 2019; Wang, Tian & Lai 2020). Despite its successful applications, the large computational cost has hindered DNS usage, especially for low Mach number flows ( $M < 0.1$ ) where the size of the time step may be restricted more by the time scale of acoustic wave propagation than by that of hydrodynamics. To address these challenges, hybrid methods (Hardin & Pope 1994; Lele 1997; Colonius & Lele 2004) have emerged as a promising approach. In these methods, the hydrodynamic field is acquired through direct solutions of the compressible or incompressible NS equations. Concurrently, the acoustic field is evaluated using simplified models (e.g. linearised Euler equations (Bailly & Juve 2000) and Green's function coupling with acoustic analogy (Lyrintzis 2003; Farassat 2007)). The hybrid methods (e.g. coupling the incompressible simulation with the acoustic analogy) could relax the time step restriction and the grid requirement for resolving the acoustic wave propagation in the DNS at low Mach number flows. Therefore, a hybrid method coupling an incompressible solver and Farassat formulation 1A is used in this work.

This work is to develop a connection between the pressure fluctuation and the vortex evolution for a 3-D hovering wing where rotational motions are involved, and a simple scaling law for noise source. The dominant vortex on the time derivative of the surface pressure and its evolution will be addressed. To achieve this, a zero-thickness low-aspect-ratio ( $AR = 1.5$ ) rectangular hovering wing at a Reynolds number of 1000 and a Mach number of 0.04 is numerically investigated by solving the incompressible NS equations with the diffused interface immersed boundary (IB) method. By using the wing model, the Farassat formulation 1A is first validated. A simplified acoustic model based on the Ffowes Williams–Hawkings (FW-H) acoustic analogy is expressed in the frequency domain and validated against the Farassat formulation 1A. Furthermore, the variation of the surface pressure is analysed and the numerical results are incorporated to illustrate

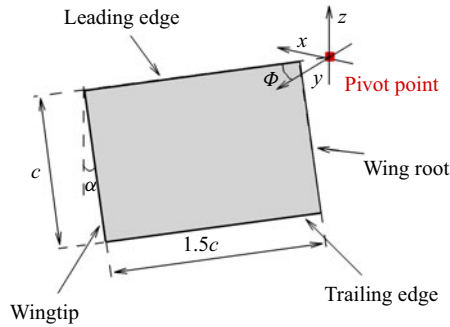


Figure 2. The schematic shows dimensions and definitions of the stroke angle ( $\Phi$ ) and the pitching angle ( $\alpha$ ) for a zero-thickness 3-D rectangular flapping wing.

the underlying relationship between the surface pressure variation and vortices evolution. Finally, a scaling analysis of the vortex acoustic source is conducted.

This paper is organised as follows. The physical model and numerical method are described in § 2 with validations, mesh and computational domain convergence studies presented in the Appendix (A). The numerical results are presented and discussed in § 3, and concluding remarks are provided in § 4.

## 2. Physical model and numerical method

### 2.1. Physical model

As shown in figure 2, a zero-thickness rectangular wing with a chord length of  $c$ , and a wingspan of  $1.5c$ , is considered. A low aspect ratio ( $AR = 1.5$ ) is used due to its high power economy and low computational cost (Shahzad *et al.* 2016). The pivot point is  $0.1c$  away from the wing root. For hovering flight, insect wings typically have three degrees of freedom (Ellington 1984). Here, we assume the wing undergoing stroke rotation around the  $z$ -axis and pitching motion around the leading edge. The stroke plane deviation is usually very small (Chen *et al.* 2016; Shahzad *et al.* 2018), and thus ignored here. The stroke and pitching motions, akin to those described in Dai, Luo & Doyle (2012), are adopted,

$$\Phi(t) = \frac{\pi}{5} \sin\left(2\pi f_o t + \frac{\pi}{2}\right), \quad \alpha(t) = \frac{\pi}{6} \sin(2\pi f_o t), \quad (2.1a,b)$$

where  $\Phi$  is the angle between the leading edge and the  $y$ -axis,  $\alpha$  is the angle between the chord line and the  $z$ -axis,  $f_o = 0.25$  is the flapping frequency and  $t$  is the time ( $f_o$  and  $t$  are normalised by  $U_{ref}$  and  $c$ ). Note that a small stroke angle is used to reduce the computational cost. According to the scaling laws and previous studies (see e.g. Lee *et al.* 2015; Wang & Tian 2020), this choice is sufficient to achieve the objective of this work.

Here, a Reynolds number ( $Re = U_{ref}c/\nu$ ) of 1000 and a Mach number ( $M = U_{ref}/c_o$ ) of 0.04 are chosen, where  $U_{ref}$  is the mean tip velocity and defined as  $4\pi/5f_o(AR + 0.1)c \approx 4cf_o$ ,  $\nu$  is the kinematic viscosity and  $c_o$  is the sound speed. The chosen Reynolds number and the Mach number fall in the range of some insects (Eldredge & Jones 2019; Hightower *et al.* 2020) and allow us to investigate the characteristic features of both flow and acoustic fields at a relatively low computational cost.

## 2.2. Numerical methods

Here the incompressible NS equations solver and the FW-H acoustic analogy are used. A simplified model based on the far-field approximation and the FW-H acoustic analogy is proposed here.

### 2.2.1. Fluid solver

As the operation speed for bio-inspired flapping wings is low (Hightower *et al.* 2020), the Mach number is much less than 1. Therefore, the fluid dynamics is governed by the dimensionless 3-D incompressible NS equations,

$$\nabla \cdot \mathbf{u} = 0, \quad (2.2)$$

$$\frac{\partial \mathbf{u}}{\partial t} + \mathbf{u} \cdot \nabla \mathbf{u} = -\nabla p + \frac{1}{Re} \nabla^2 \mathbf{u} + \mathbf{f}, \quad (2.3)$$

where  $\mathbf{u}$  is the fluid velocity,  $p$  is the pressure and  $\mathbf{f}$  is the body force. Based on previous studies (Jones & Babinsky 2010; Garmann *et al.* 2013; Eldredge & Jones 2019), the flow fields for flapping wings at a Reynolds number of 1000 are laminar. To verify that the flow is laminar at  $Re = 1000$ , our results of including the dynamic Smagorinsky (DS) model (Germano *et al.* 1991) as the subgrid model (Smagorinsky constant  $C_s$  is chosen as 0.1), not shown here, show insignificant differences (less than 1%) in the aerodynamic force coefficients from our current simulation without the DS model.

The second-order central difference is used for the spatial derivative while the second-order Crank–Nicolson method is used for time marching. The incompressible NS equations are solved by a projection method consisting of three steps: (i) the momentum equations are solved by a Jacobian-free Newton–Krylov method to obtain the intermediate velocity; (ii) the pressure is updated by solving a Poisson equation with the generalised minimal residual method where the algebraic multigrid method is used as a preconditioner; and (iii) the velocity for the current step is updated based on the solutions of the Poisson equation and the intermediate velocity. More details can be found in Calderer *et al.* (2015).

The IB method (Peskin 1972; Mittal & Iaccarino 2005; Huang & Tian 2019) is used to handle the boundary condition on the wing surface. Compared with the arbitrary Lagrangian–Eulerian method (Hirt, Amsden & Cook 1974; Farhat & Lakshminarayan 2014), the fluid grid in the IB method does not have to conform to the geometry of the solid surface or be regenerated if moving boundaries are involved. Thus, the IB method is more efficient in coping with moving boundary problems, as considered here. The flow field is discretised with non-uniform Cartesian grids, and the solid surface is discretised by triangle grids. The diffused interface IB method (Peskin 1972; Goldstein, Handler & Sirovich 1993; Peskin 2002; Huang & Tian 2019), which is easy to implement and can provide reliable solutions (Huang & Tian 2019; Huang *et al.* 2022), is used to implement the boundary condition at the fluid–structure interface. More details of this method can be found in Ji *et al.* (2022, 2024).

Here a computational domain with the dimensions  $-5c \leq x \leq 5c$ ,  $-5c \leq y \leq 5c$  and  $-5c \leq z \leq 5c$ , is used. A fine grid region ( $2c \times 1.7c \times 1.2c$ ) is discretised by uniform fine grids with its size denoted as  $\Delta_{min}$  while an outer grid region is discretised by non-uniform grids. Far-field boundary conditions are enforced at the outer boundaries while the diffused interface IB method is incorporated to achieve the no-slip boundary condition at the wing surface. The fluid solver was validated in the previous works (Ji *et al.* 2022, 2024). Convergence studies of the grid and computational domain have been conducted with details presented in the Appendix (A). Based on the convergence studies,

$\Delta_{min} = 0.01c$  and a computational domain of  $10c \times 10c \times 10c$  are used for all simulations in this work.

### 2.2.2. Acoustic solver

To consider the sound generated by a moving boundary, Ffowcs Williams & Hawkings (1969) used the generalised function and rewrote the Curle equation (Curle 1955) into the FW-H equation,

$$\left(\frac{1}{c_o^2} \frac{\partial^2}{\partial t^2} - \nabla^2\right) p'(\mathbf{x}, t) = \frac{\partial}{\partial t} [\rho_o v_n \delta(f)] - \frac{\partial}{\partial x_i} [p n_i \delta(f)] + \frac{\partial^2 H(f) T_{ij}}{\partial x_i \partial x_j}, \quad (2.4)$$

where  $\rho_o$  is the ambient density,  $v_n$  is the surface normal velocity,  $p$  is the surface pressure,  $n_i$  is the unit component of normal vector of surface,  $\delta(f)$  is the Dirac function,  $H(f)$  is the Heaviside function,  $f = 0$  denotes the moving surface and  $T_{ij}$  is the Lighthill stress tensor. Note that the three source terms on the right-hand side of (2.4) are monopole, dipole and quadrupole sources, respectively. As the contributions from the quadrupole source are less significant at a low Mach number and the monopole source can be ignored due to the zero thickness (Seo *et al.* 2019) and incompressible restriction, the integral solution of (2.4) for the dipole source, known as the Farassat formulation 1A (Farassat 2007), is given by

$$4\pi p'_L(\mathbf{x}, t) = \oint \left[ \frac{\dot{p} \cos \theta}{c_o |\mathbf{r}| (1 - M_r)^2} + \frac{p \dot{M}_r \cos \theta}{c_o |\mathbf{r}| (1 - M_r)^3} + \frac{p(M_r - M^2) \cos \theta}{|\mathbf{r}|^2 (1 - M_r)^3} + \frac{p(\cos \theta - M_n)}{|\mathbf{r}|^2 (1 - M_r)^2} \right]_{ret} dA, \quad (2.5)$$

$$p'(\mathbf{x}, t) = p'_L(\mathbf{x}, t), \quad (2.6)$$

where  $p'_L(\mathbf{x}, t)$  corresponds to the sound pressure from the dipole source,  $|\mathbf{r}| = |\mathbf{x} - \mathbf{y}|$  is the distance from the acoustic source ( $\mathbf{y}$ ) to the observation point ( $\mathbf{x}$ ),  $M_r = M_i r_i$ ,  $M_n = M_i n_i$ ,  $r_i$  is the unit component of  $\mathbf{r}$ ,  $M_i$  is the  $i$ th component of the local Mach number vector  $\mathbf{M}$ ,  $\cos \theta = r_i n_i$ ,  $dA$  is the area of a surface element, *ret* indicates the retardation time and the second-order central difference scheme is used to evaluate the time derivative ( $\dot{\cdot}$ ).

### 2.2.3. Simplified model

A simplified model can be derived for the far-field acoustics to provide a better understanding of the mechanisms of the aeroacoustic generation. Based on the above assumptions, the FW-H acoustic analogy in the far field can be approximated as follows:

$$\left(\frac{1}{c_o^2} \frac{\partial^2}{\partial t^2} - \nabla^2\right) p'(\mathbf{x}, t) \approx -\frac{\partial}{\partial x_i} [p n_i \delta(f)]. \quad (2.7)$$

Given that the acoustic wavelength up to the 10th harmonics is  $\lambda = c_o / (n f_o) = 10c$  ( $n = 10$ ) which is still much larger than the size of the wing ( $1.5c$ ), the wing can be considered as a compact source. Therefore, the far-field approximation ( $\partial / \partial x_i \approx -r_i / (|\mathbf{r}| c_o) \partial / \partial t$ , see Howe (2003)) and the free space Green's function are incorporated to obtain the sound

pressure in the time and frequency domains,

$$p'(\mathbf{x}, t) = -\frac{\partial}{\partial x_i} \oint_S \frac{pn_i \delta(f)}{4\pi|\mathbf{x} - \mathbf{y}|} dS \approx \frac{r_i}{4\pi|\mathbf{r}|^2 c_o} \dot{f}_{p_i}, \quad \dot{f}_{p_i} = \oint \dot{p} n_i dA, \quad (2.8)$$

$$p'(\mathbf{x}, \omega) \approx \frac{e^{ik|\mathbf{r}|} r_i}{4\pi|\mathbf{r}|^2 c_o} \dot{f}_{p_i}(\mathbf{y}, \omega), \quad k = \omega/c_o. \quad (2.9)$$

The above equations connect the far-field acoustic pressure with the time derivative of the pressure on the wing. Therefore, uncovering the sources of the time derivative of the pressure is of importance in understanding the aeroacoustics generated by the flapping wing. Validations of the Farassat formulation 1A and the simplified model have been conducted with details shown in the [Appendix \(A\)](#).

### 3. Results and discussions

#### 3.1. Time derivative of surface pressure force

The dominant contributor to the sound pressure in the far-field is the time derivative of the surface pressure  $\dot{p}$  and thus the time derivative of surface pressure force  $\dot{f}_{p_i}$  (see (2.8)). To discuss it,  $\dot{f}_{p_i}$  over a flapping cycle  $t/T = 0$  to 1 ( $T$  is the flapping period) is shown in [figure 3\(a\)](#). At  $t/T = 0.285$ ,  $\dot{f}_{p_i}$  in the three directions is close to zero, which will be further investigated. On the other hand, the maximum fluctuation of  $\dot{f}_{p_i}$  occurs near  $t/T = 0.42$  when  $\dot{f}_{p_x}$  achieves its minimum value while the fluctuations of other two components are also high.

The instantaneous surface pressure and its time derivative together with the vortices visualised by the  $Q$ -criterion (Jeong & Hussain 1995) over the suction side at  $t/T = 0.285$  and  $t/T = 0.42$  are presented in [figures 3\(b–d\)](#) and [3\(e–g\)](#), respectively. The  $Q$ -criterion is used here because it can be taken as the acoustics and the surface pressure variation source, as will be discussed in § 3.3. The negative pressure over the outboard region at  $t/T = 0.285$  is much larger than that at  $t/T = 0.42$  (see [figure 3b,e](#)) but no significant difference in the vortical structures between these two time steps can be identified (see [figure 3d,g](#)). In addition, a  $\Pi$ -like distribution pattern with a high negative pressure ( $p < -0.7$ , see [figure 3e](#)) can be identified in the inboard region at  $t/T = 0.42$ , which is associated with the low pressure within the LEV, RV and SV (SV1). In particular, the negative pressure near the wing root at  $t/T = 0.42$  is larger than that at  $t/T = 0.285$  due to the larger RV. At  $t/T = 0.285$ ,  $\dot{p}$  over the outboard region is positive which compensates for the negative value over the inboard region, yielding a small amplitude  $\dot{f}_{p_i}$  (see [figure 3a,c](#)). At  $t/T = 0.42$ ,  $\dot{p}$  over the suction side is generally positive, indicating that the surface pressure increases, and a region R1 with a noticeably high value is found at around a chord from the wing root (see [figure 3f](#)). Although the value of  $\dot{f}_{p_i}$  can be explained by the contours of  $\dot{p}$ , the relationship between the vortical structure evolution and  $\dot{p}$  cannot be determined from [figure 3](#). Furthermore, it should be noted that  $\dot{p}$  generally increases from the wing root to the wingtip at  $t/T = 0.285$ . However, R1 does not occur at the wingtip at  $t/T = 0.42$ , which may contain some important physical insights and shall be investigated. The LEV, as a prominent vortical component, may significantly affect  $\dot{p}$  and result in the high  $\dot{p}$  at R1 (Eldredge & Jones 2019). Therefore, the LEV circulation will be quantified and examined in the next section.



## Evolution of vortices determines aeroacoustics of a wing

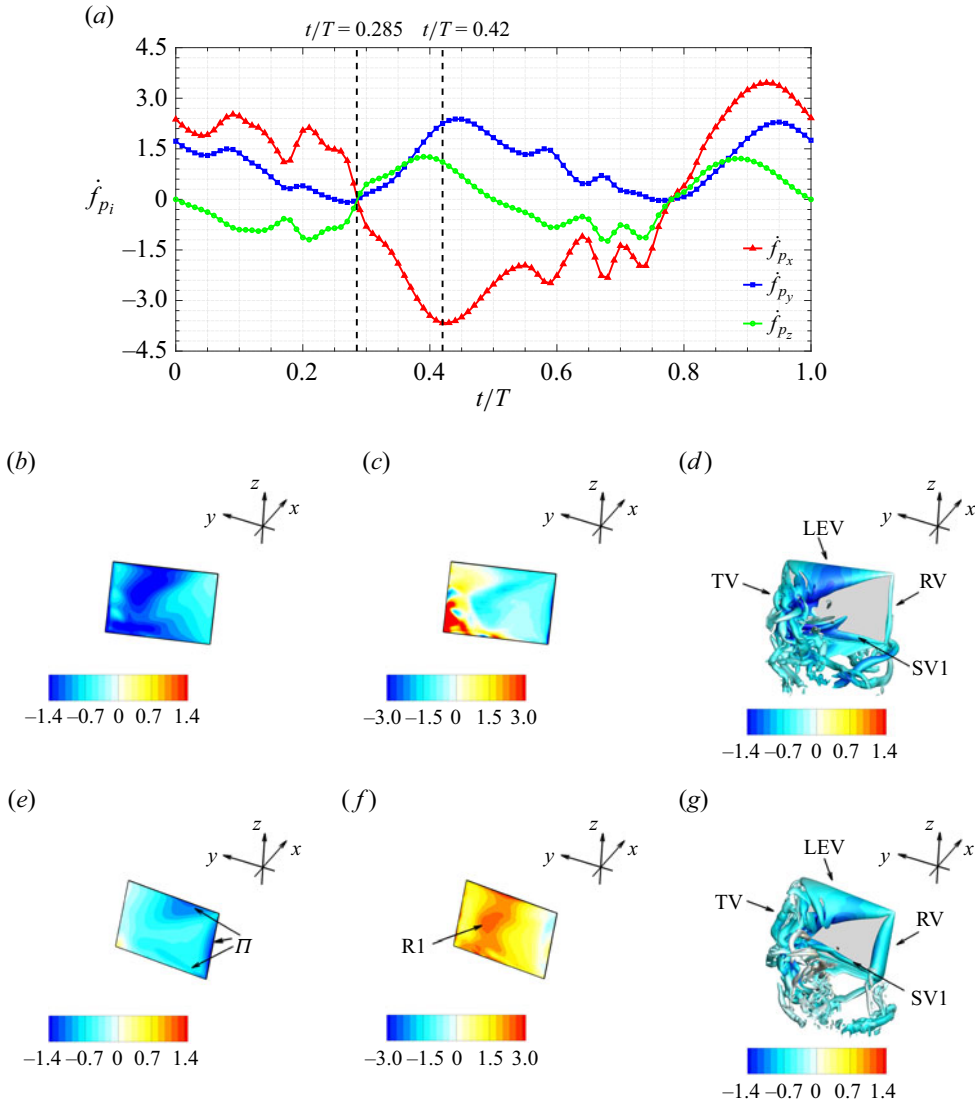


Figure 3. Force properties and vortical structures: (a) time derivative of the pressure force in the three directions; (b) instantaneous dimensionless surface pressure at  $t/T = 0.285$ ; (c) instantaneous dimensionless time derivative of the surface pressure at  $t/T = 0.285$ ; (d) vortices visualised by  $Q$ -criterion ( $Q = 30$ ) and coloured by pressure at  $t/T = 0.285$ ; (e) instantaneous dimensionless surface pressure at  $t/T = 0.42$ ; (f) instantaneous dimensionless time derivative of the surface pressure at  $t/T = 0.42$ ; (g) vortices visualised by  $Q$ -criterion ( $Q = 30$ ) and coloured by pressure at  $t/T = 0.42$ .

### 3.2. The LEV evolution

To investigate the correlation between the LEV and the high  $\dot{p}$  of R1, a body-fixed reference frame  $s$ - $n$ - $\tau$ , with its origin at the corner closest to the pivot point of the wing (see figure 4a) is first established, where  $s$  represents the direction from the trailing edge to the leading edge,  $n$  denotes the normal to the wing surface and  $\tau$  points from the wing root to the wingtip. The vorticity  $\boldsymbol{\omega} = \nabla \times \mathbf{u}$  is calculated in the  $s$ ,  $n$  and  $\tau$  directions, respectively, and the circulation of the LEV,  $\Gamma_\tau = \iint \omega_\tau \, dA$ , is defined here to quantify

the vorticity strength of the LEV and its variation near R1 (see figure 3f). In figure 4(b), the integration area  $A$  is defined as a rectangular region to exclude the contribution of the vorticity of SV1 (see figure 3d,g). Additionally, the LEV is bounded by  $Q > 0$  and  $\omega_\tau < 0$  (similar definition can be found in Chen *et al.* (2022)). Here, two slices S1 ( $\tau = 0.75c$ ) and S2 ( $\tau = 0.95c$ ) (see figure 4c,d), are chosen for calculating the LEV circulation. Here S1 is placed out of R1 while S2 crosses R1. It should be noted that the LEV will lose its coherence at the further outboard area where the tilting of the TV may affect the estimation of the LEV circulation. Therefore, the LEV circulation at the outboard region is not considered here. Apart from  $\Gamma_\tau$ , the vorticity fluxes  $\hat{\omega}_s$  and  $\hat{\omega}_n$  at S1 and S2 are obtained by integrating the other two vorticity components within the LEV region to show the strength of vorticity in the  $s$  and  $n$  directions.

Overall, it can be observed from figure 4(e) that  $\Gamma_\tau$  is larger with respect to the vorticity fluxes in the other two directions ( $\hat{\omega}_s$  and  $\hat{\omega}_n$ ) for both slices, and the values at S2 are generally larger than those at S1, suggesting that the LEV is more 3-D and unsteady near R1 over the inboard region. At S1,  $\hat{\omega}_s$  and  $\hat{\omega}_n$  have a similar variation tendency and share a similar maximum value of around 0.35 at  $t/T = 0.38$ . At S2, the variation of  $\hat{\omega}_s$  and  $\hat{\omega}_n$  is different after achieving its maximum value at  $t/T = 0.33$ . At  $t/T = 0.285$ , the variation trend of  $\Gamma_\tau$  at S1 and S2 is similar, which may explain why  $\dot{p}$  has a similar magnitude near S1 and S2 (see figure 4c). Meanwhile,  $\Gamma_\tau$  of S1 and S2 at  $t/T = 0.42$  increases, indicating a reduction of the LEV circulation, and the increase rate of  $\Gamma_\tau$  at S2 is larger with respect to that of S1, corresponding to the higher  $\dot{p}$  at R1 (see figure 4d). Moreover, the difference in the variation rate at  $t/T = 0.42$  between S1 and S2 is larger than that at  $t/T = 0.285$ .

Additionally, the cross-correlations between  $\dot{\Gamma}_\tau$ ,  $\dot{\hat{\omega}}_s$ , and  $\dot{\hat{\omega}}_n$  and  $\dot{p}$  are incorporated to investigate and quantify the relationship between the time derivatives of the pressure and vortex evolution,

$$R_{\dot{\Gamma}_\tau \dot{p}} = \frac{1}{N} \sum_{n=1}^N \frac{(\dot{\Gamma}_\tau - \overline{\dot{\Gamma}_\tau})(\dot{p} - \bar{p})}{\sigma_{\dot{\Gamma}_\tau} \sigma_{\dot{p}}}, \quad R_{\dot{\hat{\omega}}_i \dot{p}} = \frac{1}{N} \sum_{n=1}^N \frac{(\dot{\hat{\omega}}_i - \overline{\dot{\hat{\omega}}_i})(\dot{p} - \bar{p})}{\sigma_{\dot{\hat{\omega}}_i} \sigma_{\dot{p}}}, \quad i = n, s, \tag{3.1a,b}$$

where  $(\dot{\cdot})$  denotes the time derivative,  $N$  is the total sample number,  $\dot{\Gamma}_\tau$  and  $\dot{\hat{\omega}}_i$  are the time derivatives of the LEV circulation and vorticity fluxes of the LEV in the  $n$  and  $s$  directions at S2,  $(\bar{\cdot})$  denotes the average values and  $\sigma_{\square}$  denotes the root mean square (r.m.s.) value.

Three points (P<sub>S1</sub>, P<sub>S2</sub> and P<sub>S3</sub>) located at the intersection of three slices with the midchord of the wing (see figure 4c,d) have been selected to investigate as the midchord line crosses R1. It is believed that P<sub>S1</sub> and P<sub>S2</sub> are significantly influenced by the evolution of the LEV, while P<sub>S3</sub> is chosen for comparison as it is less influenced by the LEV. Here  $R_{\dot{\Gamma}_\tau \dot{p}}$  and  $R_{\dot{\hat{\omega}}_i \dot{p}}$  over  $t/T = 0$  to 0.5 at the three points are summarised in table 1. The sample number  $N$  is 50 with an interval of  $0.01T$ . Here  $R_{\dot{\Gamma}_\tau \dot{p}}$  at P<sub>S1</sub> and P<sub>S2</sub> is high (with absolute values larger than 0.8), indicating that the time derivative of surface pressure at these two points is significantly related to the variation of the LEV circulation. Here  $R_{\dot{\hat{\omega}}_s \dot{p}}$  and  $R_{\dot{\hat{\omega}}_n \dot{p}}$  share a similar value at P<sub>S1</sub> while  $R_{\dot{\hat{\omega}}_n \dot{p}}$  ( $-0.79$ ) is more significant than  $R_{\dot{\hat{\omega}}_s \dot{p}}$  ( $-0.67$ ) at P<sub>S2</sub>. One possible explanation is that the dual stage vortex tilting for the flapping wing (see Chen, Cheng & Wu (2023a); Chen *et al.* (2023b) for more information) have reoriented the LEV and converted the vorticity from the  $\tau$  axis to the  $n$  axis. Conversely, a weak cross-correlation is observed at P<sub>S3</sub>, suggesting that the pressure variation in the outboard region is less influenced by the LEV, which loses its coherence near the wingtip.

## Evolution of vortices determines aeroacoustics of a wing

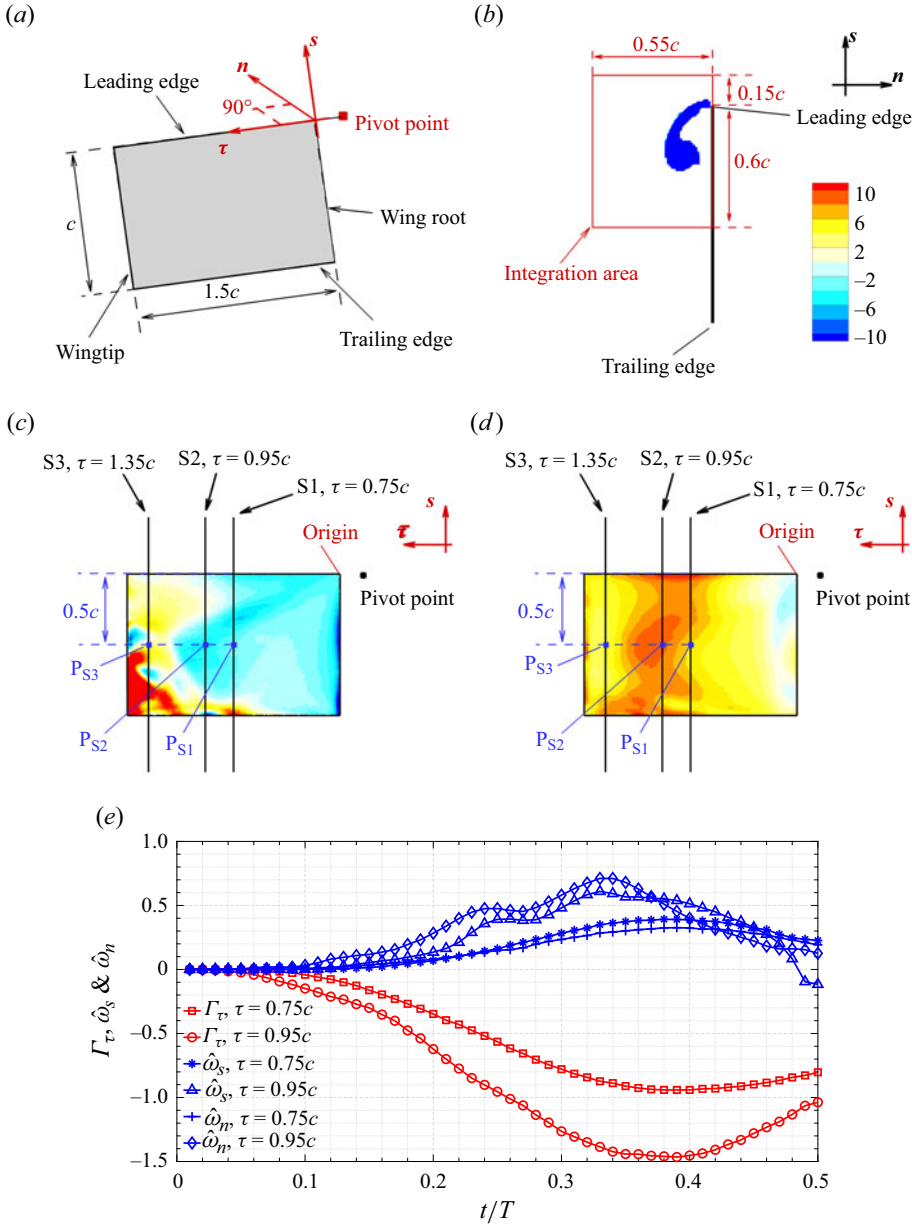


Figure 4. The LEV structures: (a) schematic of the body-fixed reference frame  $s$ - $n$ - $\tau$  (marked by the red colour); (b) schematic of circulation integration area and the LEV is highlighted by the contours of  $\omega_\tau$ ; (c) schematics of S1–3, with the contours of  $\dot{p}$  at  $t/T = 0.285$ ; (d) schematics of S1–3, with the contours of  $\dot{p}$  at  $t/T = 0.42$ ; (e) the LEV circulation  $\Gamma_\tau$ , and vorticity fluxes  $\dot{\omega}_s$  and  $\dot{\omega}_n$  of S1 and S2.

### 3.3. Analytical analysis on the vortices and the time derivative of the surface pressure

From the previous section, the evolution of the LEV has been identified as an important factor in determining the time derivative of the surface pressure. Here, the role of the vortices evolution on the time derivative of the surface pressure is further investigated. To do so, an analytical expression of the time derivative of the surface pressure is established

	$R_{\dot{\omega}_s \dot{p}}$	$R_{\dot{\omega}_n \dot{p}}$	$R_{\dot{\Gamma}_\tau \dot{p}}$
PS <sub>1</sub>	-0.71	-0.73	0.84
PS <sub>2</sub>	-0.67	-0.79	0.83
PS <sub>3</sub>	-0.35	-0.16	0.15

Table 1. Cross-correlation between  $\hat{\omega}_s$ ,  $\hat{\omega}_n$  and  $\dot{\Gamma}_\tau$  at S2 and  $\dot{p}$  of PS<sub>1</sub>, PS<sub>2</sub> and PS<sub>3</sub>.

with all source terms placed on the right-hand side of the expression. An analysis is conducted to investigate the relationship between the source terms and vortices evolution by incorporating the simulation results. To obtain the expression, the time derivative of the divergence of the momentum equations in conjugation with the incompressible restriction expressed in the body-fixed reference frame  $s-n-\tau$  (Batchelor 1967; Garmann *et al.* 2013; Jardin & David 2015) is as follows:

$$\nabla^2 \frac{\partial p}{\partial t} = \rho \left( 2 \frac{\partial \hat{Q}}{\partial t} - \underbrace{\frac{\partial[\nabla \cdot (\dot{\boldsymbol{\Omega}} \times \mathbf{r}_o)]}{\partial t}}_{\text{Angular acceleration}} - \underbrace{\frac{\partial[\nabla \cdot (\boldsymbol{\Omega} \times (\boldsymbol{\Omega} \times \mathbf{r}_o))]}{\partial t}}_{\text{Centrifugal acceleration}} - \underbrace{\frac{\partial[\nabla \cdot (2\boldsymbol{\Omega} \times \mathbf{v})]}{\partial t}}_{\text{Coriolis acceleration}} \right), \quad (3.2)$$

where  $\boldsymbol{\Omega}$  is the rotation rate of the flapping and pitching motions,  $\mathbf{r}_o$  is the vector from the rotation centre to a given point,  $\mathbf{v} = \mathbf{u} - \boldsymbol{\Omega} \times \mathbf{r}_o$  is the relative velocity and  $\hat{Q} = -1/2(\nabla \mathbf{v} : \nabla \mathbf{v})$  which is analogous to the  $Q$ -criterion for incompressible flow ( $Q = -1/2(\nabla \mathbf{u} : \nabla \mathbf{u})$ , see Jeong & Hussain (1995)).

In (3.2), the divergence of the term  $\boldsymbol{\Omega} \times \mathbf{r}_o$  is zero. Additionally, it should be noted that the centrifugal acceleration term  $-4\boldsymbol{\Omega} \cdot \dot{\boldsymbol{\Omega}}$  is a constant over the flow field. As the flapping amplitude and frequency are low, it is negligible compared with the Coriolis acceleration (also reported by Garmann *et al.* (2013)). Therefore, (3.2) can be simplified as

$$\nabla^2 \frac{\partial p}{\partial t} = \rho \left( 2 \frac{\partial \hat{Q}}{\partial t} + 4\boldsymbol{\Omega} \cdot \dot{\boldsymbol{\Omega}} - \frac{\partial[\nabla \cdot (2\boldsymbol{\Omega} \times \mathbf{v})]}{\partial t} \right) \approx 2\rho \left( \frac{\partial \hat{Q}}{\partial t} - \frac{\partial[\nabla \cdot (\boldsymbol{\Omega} \times \mathbf{v})]}{\partial t} \right). \quad (3.3)$$

From (3.3), the time derivatives of  $\hat{Q}$  and the divergence of the Coriolis acceleration are the major sources of the Poisson equation of  $\dot{p}$ . Furthermore, Green's second identity is incorporated and yields the following equation:

$$\begin{aligned} & \iiint G(\mathbf{r}, \mathbf{r}') \nabla^2 \frac{\partial p}{\partial t} - \frac{\partial p}{\partial t} \nabla^2 G(\mathbf{r}, \mathbf{r}') \, dV' \\ &= \iint G(\mathbf{r}, \mathbf{r}') \frac{\partial}{\partial n} \left( \frac{\partial p}{\partial t} \right) - \frac{\partial p}{\partial t} \frac{\partial G(\mathbf{r}, \mathbf{r}')}{\partial n} \, dS', \quad \nabla^2 G(\mathbf{r}, \mathbf{r}') = \delta(\mathbf{r} - \mathbf{r}'), \end{aligned} \quad (3.4)$$

where  $G(\mathbf{r}, \mathbf{r}')$  is Green's function,  $\mathbf{r}$  is the observer location,  $\mathbf{r}'$  is the source location,  $\delta(\mathbf{r} - \mathbf{r}')$  is the Dirac function,  $dV'$  is the flow domain and  $dS'$  is the wing surface. In the body-fixed reference frame, the two terms on the right-hand side of (3.4),  $\partial/\partial n(\partial p/\partial t)$  and  $\partial G(\mathbf{r}, \mathbf{r}')/\partial n$ , are almost zero if the volume is properly selected. The solution of (3.3)

is approximated as

$$\frac{\partial p(\mathbf{r})}{\partial t} \approx 2\rho \iiint G(\mathbf{r}, \mathbf{r}') \left[ \frac{\partial \hat{Q}(\mathbf{r}')}{\partial t} - \frac{\partial [\nabla \cdot (\boldsymbol{\Omega} \times \mathbf{v}(\mathbf{r}'))]}{\partial t} \right] dV', \quad (3.5)$$

which indicates that the surface pressure derivative is related to  $\partial \hat{Q}/\partial t$  and  $\partial [\nabla \cdot (\boldsymbol{\Omega} \times \mathbf{v})]/\partial t$  in the body-fixed reference frame. The two terms on the right-hand side of (3.5) at S1–3 (see figure 4) of  $t/T = 0.285$  and  $t/T = 0.42$  are presented in figure 5. It should be noted that S3 is included here as  $\dot{p}$  at  $t/T = 0.285$  near S3 is much larger than that of the inboard region, implying that investigating S3 is physically meaningful.

At  $t/T = 0.285$  (see figure 5a–f), the Coriolis acceleration term  $\partial [\nabla \cdot (\boldsymbol{\Omega} \times \mathbf{v})]/\partial t$  is much lower with respect to  $\partial \hat{Q}/\partial t$  in the three slices. Generally, it can be found that the region with high  $\partial \hat{Q}/\partial t$  is mainly enclosed by the boundary of  $Q = 0$  (marked by the solid black line, considered as the boundary of vortical structures), which indicates that  $\partial \hat{Q}/\partial t$  arises from vortices evolution. It can be seen that the LEV grows in size from S1 to S2. Furthermore,  $\partial \hat{Q}/\partial t$  in the proximity of the wing surface is negative due to the absorption of the SV (SV2). In contrast,  $\partial \hat{Q}/\partial t$  at the outer side of the LEV is positive due to the vorticity fed by the shear layer emanating from the leading edge. The similar distribution pattern of  $\partial \hat{Q}/\partial t$  leads to the similar  $\dot{p}$  at the wing surface for S1 and S2. At S3,  $\partial \hat{Q}/\partial t$  near the wing surface is less prominent but much higher in the wake region where the complex and unsteady vortical interaction (see figure 3d) may account for the higher  $\partial \hat{Q}/\partial t$ . The different distribution patterns and magnitudes of  $\partial \hat{Q}/\partial t$  account for the difference in  $\dot{p}$  between S3 and the inner region.

At  $t/T = 0.42$  (see figure 5g–l), the Coriolis acceleration term is also much less significant than  $\partial \hat{Q}/\partial t$ , suggesting that  $\dot{p}$  is dominated by the latter. Here  $\partial \hat{Q}/\partial t$  within the LEV for S1 and S2 is larger than that at  $t/T = 0.285$  and the LEV begins to detach and moves downstream. The effects of the variation of the distance between the wing surface ( $\mathbf{r}$ ) and the source location ( $\mathbf{r}'$ ) are represented by changing the value of  $G(\mathbf{r}, \mathbf{r}')$  in the integration of (3.5) and lead to the variation of  $\dot{p}$ , which will be discussed in the next section. At S3, the high-value region of  $\partial \hat{Q}/\partial t$  moves upwards compared with that of  $t/T = 0.285$ . Overall,  $\partial \hat{Q}/\partial t$  within the LEV of S1 is less than that of S2, which correlates with the lower  $\dot{p}$  at the wing surface near S1. Although the high  $\partial \hat{Q}/\partial t$  in the wake region of S3 is comparable with that within the LEV of S2, its larger distance from the wing surface renders its influences less significant, which may explain the lower  $\dot{p}$  near S3 than that of R1.

### 3.4. Position of the LEV

Despite the presence of both  $\partial \hat{Q}/\partial t$  and the Coriolis acceleration terms, Green's function in (3.4) may play an important role in the formation of R1 and will be elaborated upon here. Green's function  $G(\mathbf{r}, \mathbf{r}')$  is related to the distance between the source  $\mathbf{r}'$  and the wing surface  $\mathbf{r}$ , but its expression cannot be readily given here. In the body-fixed reference frame,  $\mathbf{r}$  is set as stationary and the only variable in Green's function is  $\mathbf{r}'$ . This indicates that Green's function can be evaluated by reflecting on the source location. From previous section, it is found that  $\partial \hat{Q}/\partial t$  within the LEV is the dominant source for R1 (see figure 5h). Therefore, it can be summarised that the effects of Green's function can be reflected by evaluating the location of the LEV (bounded by  $Q > 0$  and  $\omega_\tau < 0$ ). In figure 6(a), the LEV with the contours of  $Q$  at four specific time steps ( $t/T = 0.1, 0.2, 0.42$  and  $0.49$ ) is

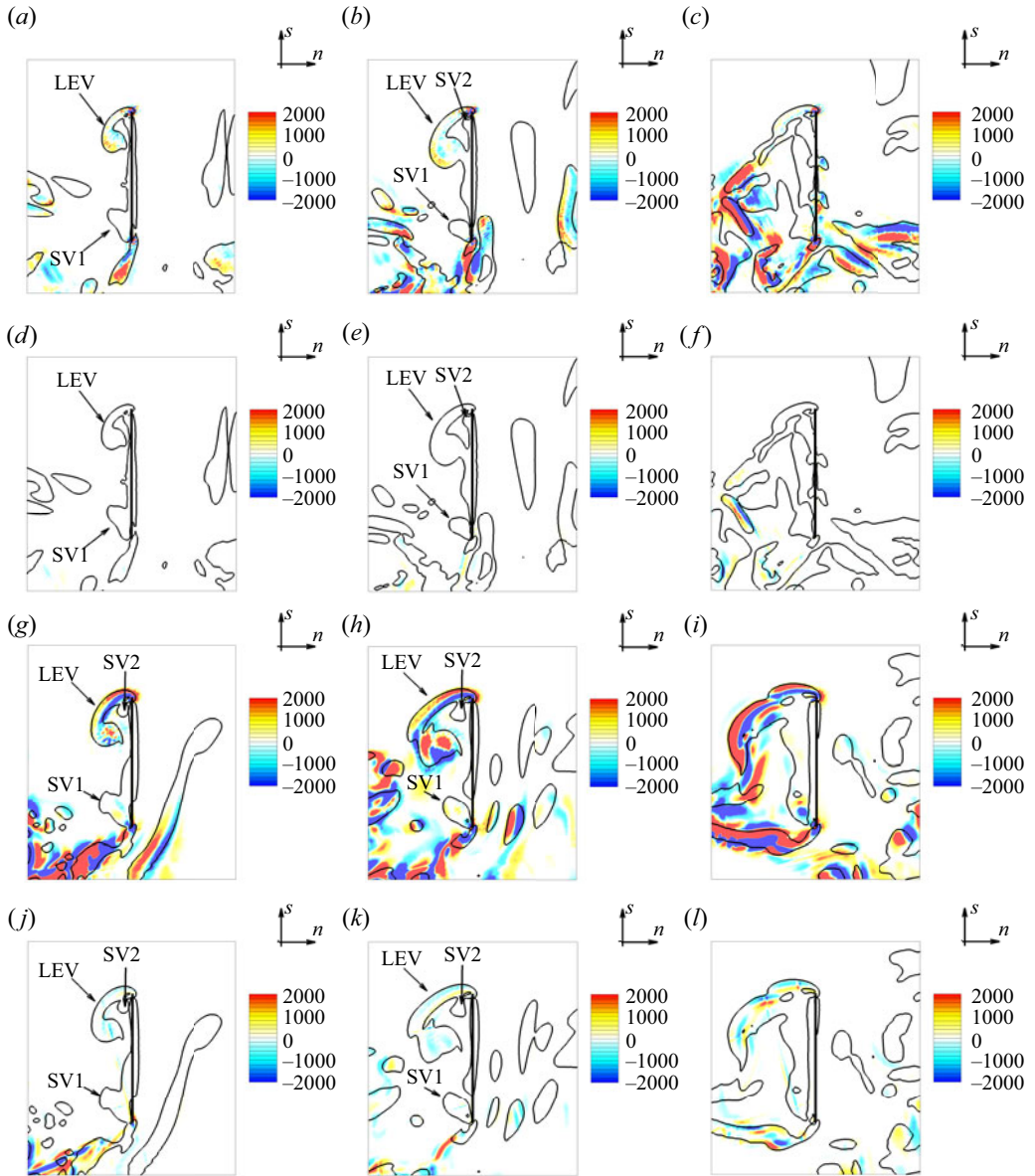


Figure 5. Partial derivative  $\partial\hat{Q}/\partial t$  ( $Q = 0$  marked by the black line) at (a) S1, (b) S2 and (c) S3 of  $t/T = 0.285$ ; Coriolis acceleration term at (d) S1, (e) S2 and (f) S3 of  $t/T = 0.285$ ;  $\partial\hat{Q}/\partial t$  at (g) S1, (h) S2 and (i) S3 of  $t/T = 0.42$ ; Coriolis acceleration term at (j) S1, (k) S2 and (l) S3 of  $t/T = 0.42$ .

shown. Generally, it can be found that the LEV increases its size and moves downward and backward from  $t/T = 0.1$  to  $0.4$ , while less variation can be identified between  $t/T = 0.4$  and  $0.49$ . Furthermore, the location of the LEV should be quantified. Analogous to the concept of the centroid of vorticity (Huang & Green 2015; Jones *et al.* 2016), the centroid

of  $Q$  of the LEV is used to represent the source location and given as follows:

$$Q_s = \frac{\iint sQ \, dA}{\iint Q \, dA}, \quad Q_n = \frac{\iint nQ \, dA}{\iint Q \, dA}, \quad (3.6a,b)$$

where  $Q_s$  and  $Q_n$  are the coordinates of the centroid of the  $Q$  within the LEV in the  $s$  and  $n$  directions, respectively, and  $A$  is the region of the LEV (defined in § 3.2).

The  $Q$  centroid of the LEV at S2 ( $\tau = 0.95c$ ) from  $t/T = 0.05$  to  $0.5$  is shown in figure 6(b,c). Note that the leading edge is located at  $(s, n) = (0, 0)$ . From figure 6(a), it can be observed that the LEV generally moves from the leading edge to the trailing edge, detaching from the wing surface to downstream. However, the opposite trend can be found near the end of the half-stroke. The time histories of  $Q_s$  and  $Q_n$  are shown in figure 6(c) and the extreme values occur near  $t/T = 0.42$  corresponding to the high  $\dot{p}$  for R1, as shown in figure 3. Another interpretation of the formation of R1 is that the detachment of the LEV and the variation of  $\hat{Q}$  increase the surface pressure, resulting in a high positive  $\dot{p}$  at R1.

### 3.5. A scaling law for the vortex acoustic source

As discussed in the Section 3.3,  $\partial\hat{Q}/\partial t$  arising from the vortical structures evolution is considered as the main source for  $\partial p/\partial t$  which is considered as the dominant source of the far-field noise generated by the hovering wing (see (2.9)). In other words,  $\partial\hat{Q}/\partial t$  can be regarded as the noise source from vortex evolution. It is thus worthy to scale the magnitude of  $\partial\hat{Q}/\partial t$  and  $\partial p/\partial t$  with kinematic parameters (e.g.  $f_0$ ) to provide a new insight for MAV design.

According to Lee *et al.* (2015), the vorticity within the LEV of a flapping wing is estimated by

$$\omega \sim \frac{U_{ref} c AR \sin(\alpha)}{A_{vor}(AR + 2)}, \quad (3.7)$$

where  $A_{vor}$  is the cross area of the vortex, and  $\alpha$  is the angle of attack during the middle stroke. Therefore,  $\hat{Q}$  can be estimated as

$$\hat{Q} \simeq \frac{1}{4}\omega^2 \sim \frac{U_{ref}^2 c^2 AR^2 \sin^2(\alpha)}{4A_{vor}^2 (AR + 2)^2} = \frac{4\pi^2 c^4 AR^2 (AR + 0.1)^2 \sin^2(\alpha)}{25A_{vor}^2 (AR + 2)^2} f_0^2, \quad (3.8)$$

where  $U_{ref} = 4\pi(AR + 0.1)cf_0/5$  is applied. The change of  $\hat{Q}$  happens within a period of flapping, and thus

$$\frac{\partial\hat{Q}}{\partial t} \sim \frac{4\pi^2 c^4 AR^2 (AR + 0.1)^2 \sin^2(\alpha)}{25A_{vor}^2 (AR + 2)^2} f_0^3. \quad (3.9)$$

The scaling law for the pressure variation with respect to time is achieved by applying (3.9) into (3.5), i.e.

$$\frac{\partial p}{\partial t} \sim A_{vor} \partial\hat{Q}/\partial t \sim \frac{4\pi^2 c^4 AR^2 (AR + 0.1)^2 \sin^2(\alpha)}{25A_{vor} (AR + 2)^2} f_0^3. \quad (3.10)$$

The r.m.s. values of  $f_{p_i}$  (see (2.8)) are incorporated here as an indicator to show whether the  $f_0^3$  law is valid. Here, five different flapping frequencies are chosen as

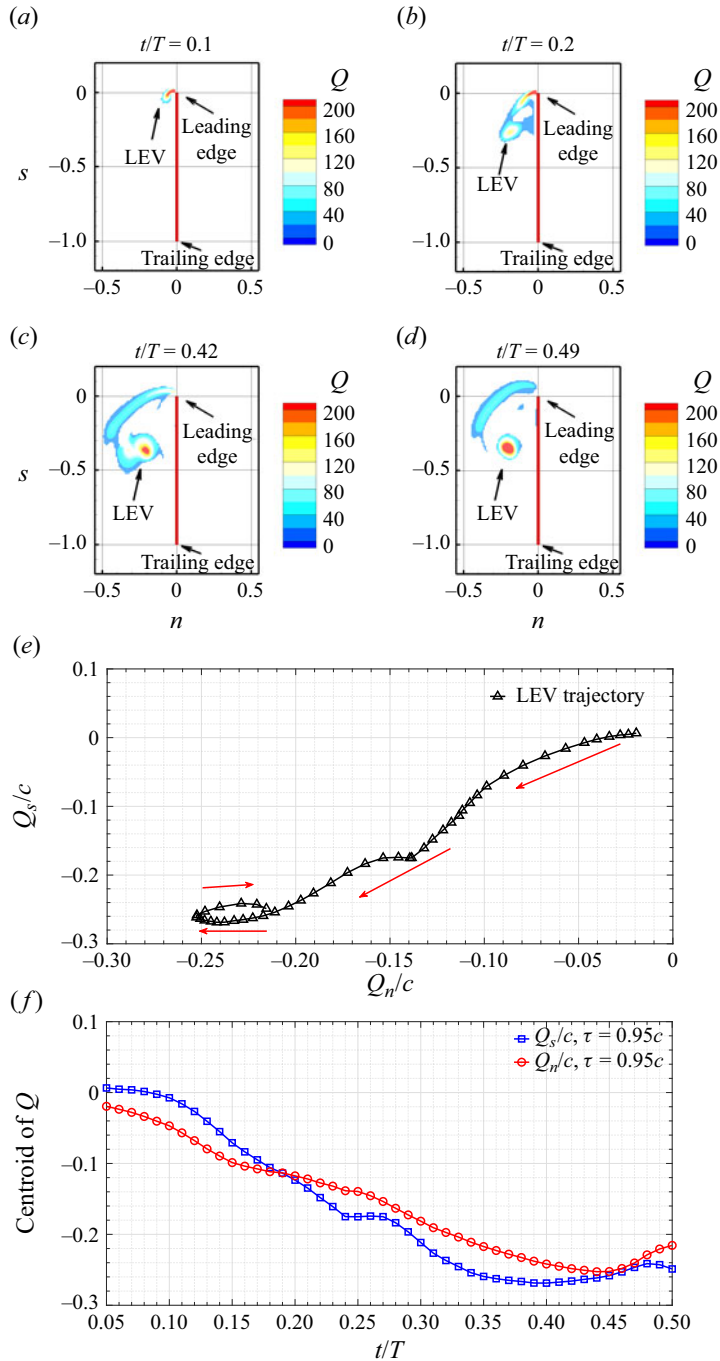


Figure 6. Vortex evolution: (a–d) contours of  $Q$  within the LEV region at  $t/T = 0.1, 0.2, 0.42$  and  $0.49$ , respectively; (e) LEV trajectory at  $S_2 \tau = 0.95c$ , represented by the centroid of  $Q$  (red arrow denotes the LEV evolution direction); (f) time histories of the centroid of  $Q$  ( $Q_s$  and  $Q_n$ ) at  $S_2$  from  $t/T = 0.05$  to  $0.5$ .



## Evolution of vortices determines aeroacoustics of a wing

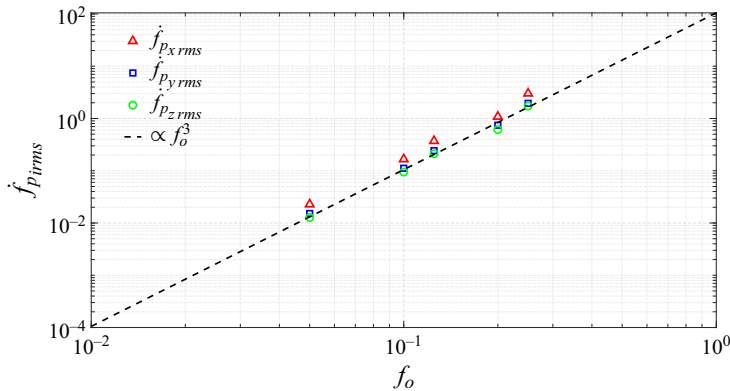


Figure 7. Scaling law for the time derivatives of pressure forces.

$f_o = \{0.05, 0.1, 0.125, 0.2, 0.25\}$ , yielding five different Reynolds numbers ranging from 200 to 1000. Here  $f_{p_i}$  is calculated after twenty flapping cycles where the cycle-to-cycle variations in the pressure are negligible. The second-order central difference is adopted to calculate the time derivative of the surface pressure. The r.m.s. values of  $f_{p_i}$  are evaluated over five flapping cycles as shown in figure 7, where the r.m.s. of  $f_{p_i}$  is proportional to  $f_o^3$  for all three directions. The coefficients in (3.9) and (3.10) appear as a minor shift in the vertical direction, and thus are not explicitly included. Therefore, the vortex acoustic source  $\partial \hat{Q} / \partial t$  is scaled by  $f_o^3$ . It should be noted that the scaling law, (3.10), is a very useful tool in MAV design and other engineering applications.

## 4. Conclusions

The influences of the evolution of vortices on the aeroacoustics of a hovering rectangular wing with a low aspect ratio of 1.5 at Reynolds number of 1000 and Mach number of 0.04 is numerically investigated using a 3-D NS equation solver and diffused interface IB method. A simplified acoustic model based on the FW-H acoustic analogy suggests that the time derivative of the surface pressure ( $\dot{p}$ ) is the dominant noise source for the far-field acoustics. A body-fixed reference frame  $s-n-\tau$ , with its origin placed at the corner closest to the pivot point of the flapping wing is considered. The variations of the LEV circulation and vorticity fluxes calculated at two spanwise slices S1 ( $\tau = 0.75c$ ) and S2 ( $\tau = 0.95c$ ) show that they are related to the variation of  $\dot{p}$  based on the cross-correlation analysis. Particularly, a region with high  $\dot{p}$  caused by the interaction (vortex tilting effects) between the LEV and the TV is identified near S2, suggesting that the vortices interaction can amplify the noise source. Moreover, the formulation for the  $\dot{p}$  in the body-fixed reference frame for the flapping wing is obtained by incorporating Green's function. The time derivatives of the  $Q$ -value in the body-fixed reference frame ( $\partial \hat{Q} / \partial t$ , representing the divergence of the convection), the angular acceleration and the Coriolis acceleration determine the time derivative of the surface pressure. Further investigation suggests that  $\partial \hat{Q} / \partial t$  arising from vortical structure evolution (especially for the LEV), is the dominant source, which overrides the influences of angular and Coriolis accelerations. The position of the LEV at S2 is calculated finding that the shedding of the LEV together with the large magnitude  $\partial \hat{Q} / \partial t$  results in the increase of the surface pressure and the high  $\dot{p}$ . The analytical framework established in this work can be further extended to investigate

Case	$\Delta_{min}$	Total grids
Coarse	$0.032c$	$138 \times 127 \times 110$
Medium	$0.016c$	$195 \times 176 \times 151$
Fine	$0.008c$	$320 \times 280 \times 230$

Table 2. Grid convergence study.

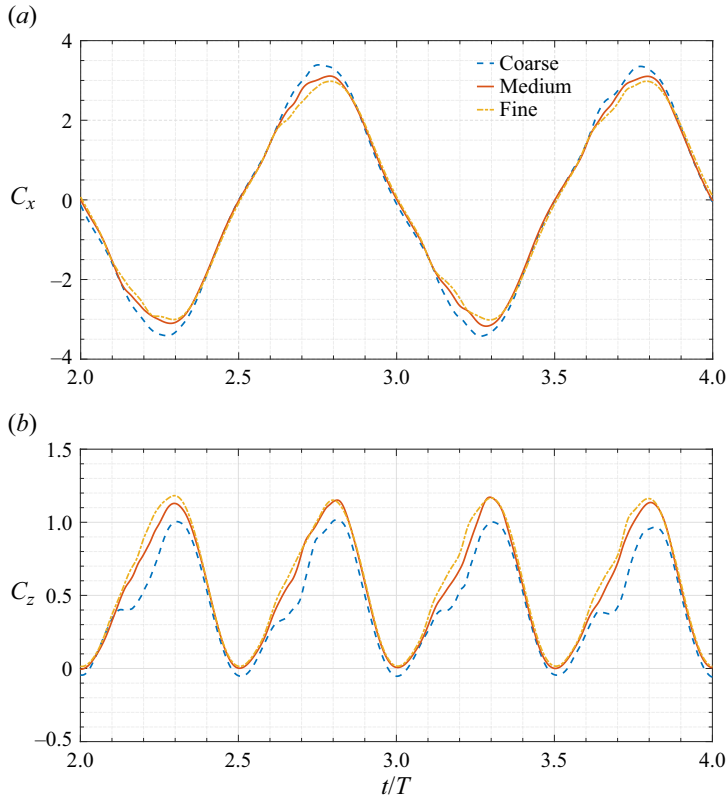


Figure 8. Grid convergence study: (a) instantaneous force coefficient in the  $x$ -axis  $C_x$  and (b) instantaneous force coefficient in the  $z$ -axis  $C_z$ , obtained from the coarse, medium and fine grids.

the noise sources for other rotating compact surfaces (e.g. UAV propellers). A scaling analysis shows that the vortex acoustic source  $\partial \hat{Q} / \partial t$  is scaled by  $f_o^3$ . Further parametric investigations of the wing, such as variations in aspect ratio, stroke angle and Reynolds number, could be conducted in future work to gain deeper insight into the relationship between vortex evolution and surface pressure fluctuations.

**Acknowledgements.** The computation work of this research was performed on the National Computational Infrastructure (NCI) supported by the Australian Government. This work was supported by the Australian Research Council Discovery Project (grant no. DP200101500). The authors would like to thank Dr D. Petty and Dr K. Talluru Murali at UNSW Canberra for their insightful discussions.

**Declaration of interests.** The authors report no conflict of interest.

## Evolution of vortices determines aeroacoustics of a wing

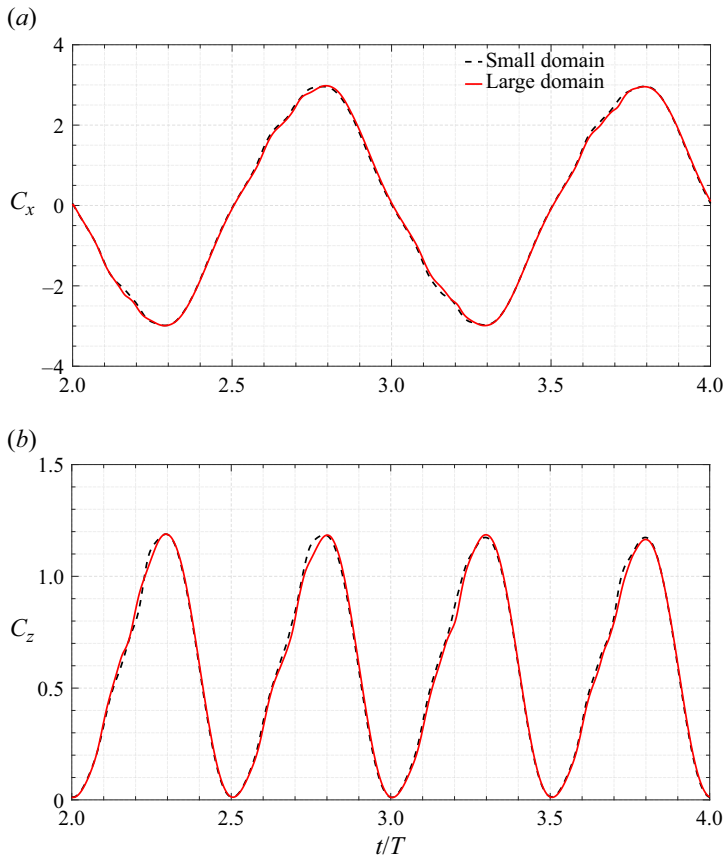


Figure 9. Computational domain convergence study: (a) instantaneous force coefficient in the  $x$ -axis  $C_x$  and (b) instantaneous force coefficient in the  $z$ -axis  $C_z$ , obtained from small and large computational domains.

### Author ORCIDs.

-  Bruce Ruishu Jin <https://orcid.org/0009-0009-8873-110X>;
-  John Young <https://orcid.org/0000-0002-8671-990X>;
-  Joseph C.S. Lai <https://orcid.org/0000-0002-8946-9993>;
-  Fang-Bao Tian <https://orcid.org/0000-0002-1247-6896>.

## Appendix A. Numerical validation

### A.1. Grid convergence study

Three different sizes of grids are used here as listed in table 2. The size of the solid surface grid of the wing is chosen as the same as the fluid grid for each scenario. Twenty flapping cycles have been simulated, which is sufficient to ensure the flow field does not change significantly from cycle to cycle. Furthermore, the instantaneous force coefficients along the  $x$ -axis ( $C_x = 2F_x/(\rho_0 U_{ref}^2 1.5c^2)$ ,  $F_x$  is the force along the  $x$ -axis) and  $z$ -axis ( $C_z = 2F_z/(\rho_0 U_{ref}^2 1.5c^2)$ ,  $F_z$  is the force along the  $z$ -axis) obtained from these three different grids are shown in figure 8 where the results from the medium and fine grids are closer with respect to that from the coarse grid. Therefore, it can be concluded that the medium

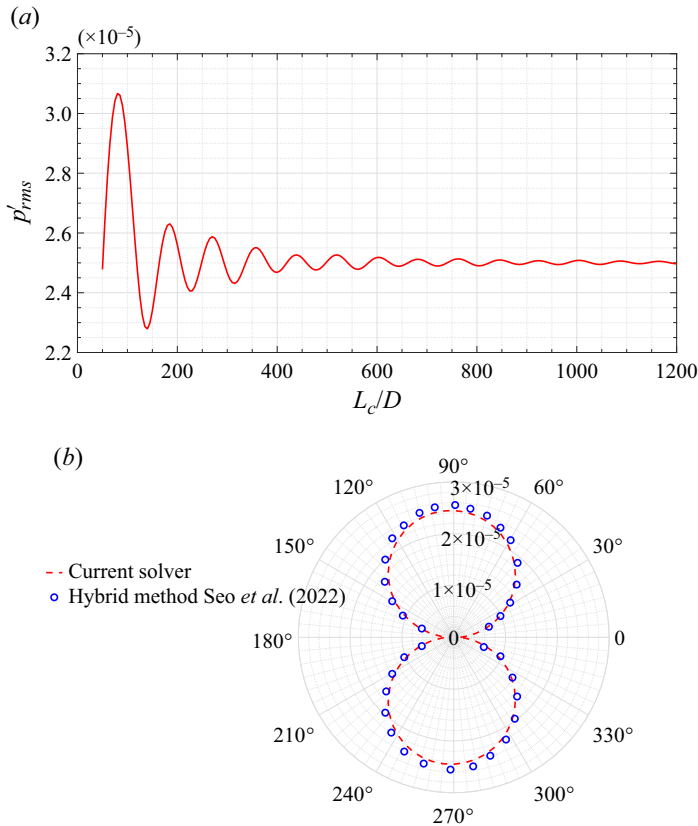


Figure 10. Sound pressure generated by a 2-D heaving circular cylinder at  $Re = 100$  and  $M = 0.1$ : (a) r.m.s. of sound pressure at  $(0, 50D, 0)$  obtained from different spanwise extension length ( $L_c$ ) and (b) r.m.s. of sound pressure at  $|r| = 50D$  obtained from current solver with  $L_c = 1100D$  and the results from Seo *et al.* (2022) are used here for comparison.

grid is considered to be fine enough to calculate the flow field here. Here  $\Delta_{min}$  of  $0.01c$  will be used in all simulations to achieve a higher resolution at a reasonable cost.

### A.2. Computational domain convergence study

Two different computational domains were selected: (i) a small computational domain ( $10c \times 10c \times 10c$ ) and (ii) a large computation domain ( $20c \times 20c \times 20c$ ). With the same grid resolution used in fine grid region ( $\Delta_{min} = 0.01c$ ), the total grid points for these two domains are 11 362 000 and 25 740 000, respectively. The instantaneous force coefficients  $C_x$  and  $C_z$  (see figure 9) are insignificantly affected (less than 1% variation). Therefore, the small computational domain is used in this work.

### A.3. Farassat formulation 1A validation

To validate the acoustic solver, the acoustic field generated by a 2-D periodic oscillating circular cylinder in a uniform flow with a prescribed motion in the  $y$  direction of  $y(t) = 0.1D \sin(2\pi \cdot 0.25t)$  is calculated. The Reynolds number (based on the velocity of the incoming flow  $U_o$  and the diameter of the cylinder  $D$ ) and the Mach number are 100

## Evolution of vortices determines aeroacoustics of a wing

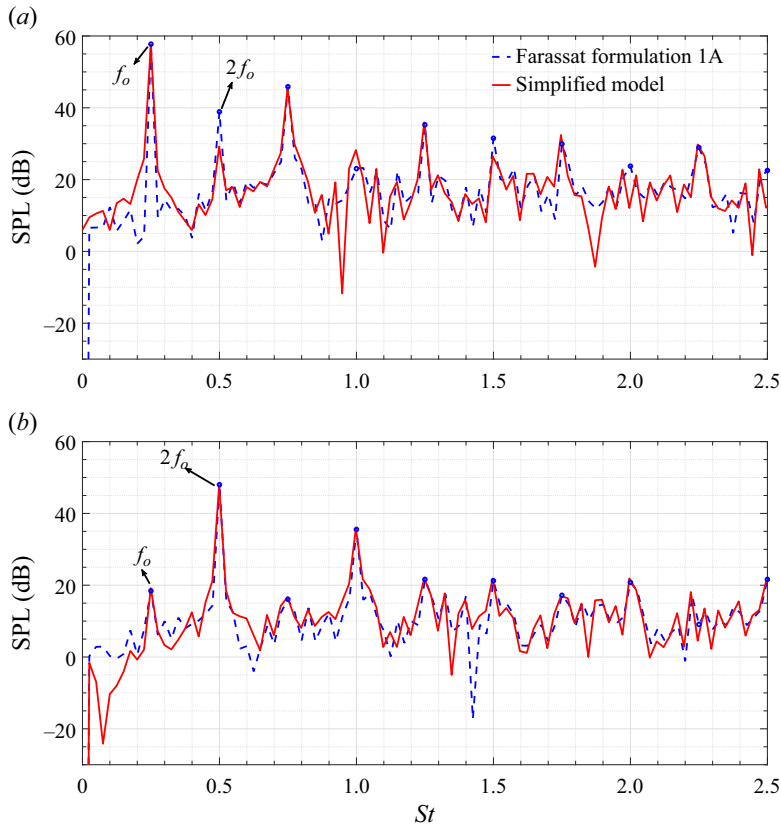


Figure 11. Sound pressure level (SPL) in the frequency domain at (a)  $(100c, 0, 0)$  and (b)  $(0, 0, 100c)$ , obtained from the Farassat formulation 1A and the simplified model,  $St = fc/U_{ref}$ .

and 0.1, respectively. To compare the results from the current acoustic solver with those from the 2-D simulation, a spanwise extension of the noise sources (Singer *et al.* 2000) is used here. The r.m.s. of the sound pressure (normalised by  $\rho_o$  and  $c_o$ ) at  $(0, 50D, 0)$  normal to the incoming flow is calculated by varying the spanwise extension length  $L_c$  and shown in figure 10(a) where  $p'_{rms}$  converges to  $2.5 \times 10^{-5}$  at a large  $L_c$  (e.g.  $L_c/D > 1000$ ). Therefore,  $L_c = 1100D$  is chosen here. The r.m.s. values of the sound pressure at  $|r| = 50D$  from the current solver are in good agreement with that from Seo *et al.* (2022) as shown in figure 10(b).

### A.4. Simplified model validation

To validate the simplified model [see (2.9)], the sound pressure generated by the hovering wing (see figure 2) at  $(100c, 0, 0)$  and  $(0, 0, 100c)$  obtained from the simplified model is compared with that from the Farassat formulation 1A (see (2.6), results are transformed into the frequency domain via fast Fourier transform) in figure 11. The input for the simplified model and Farassat formulation 1A is the fluid data that are obtained from 10 flapping cycles and collected every 10 time steps ( $10\Delta t = 0.04$ ), yielding a resolution in the frequency domain of  $\Delta St = 0.025$ . It can be seen that good agreement between these two methods has been achieved with some discrepancies at  $2f_o$  for  $(100c, 0, 0)$  (see figure 11a), which may be caused by the fact that the  $2f_o$  component dominates the noise

at the sides ( $y$ - and  $z$ -directions). Overall, the simplified model with its low computational cost and excellent accuracy has proven that the time derivative of the surface pressure is the dominant noise source for the hovering wing at a low Mach number.

## REFERENCES

- ARTHUR, B.J., EMR, K.S., WYTENBACH, R.A. & HOY, R.R. 2014 Mosquito (*Aedes aegypti*) flight tones: frequency, harmonicity, spherical spreading, and phase relationships. *J. Acoust. Soc. Am.* **135** (2), 933–941.
- BAE, Y. & MOON, Y.J. 2008 Aerodynamic sound generation of flapping wing. *J. Acoust. Soc. Am.* **124** (1), 72–81.
- BAILLY, C. & JUVE, D. 2000 Numerical solution of acoustic propagation problems using linearized Euler equations. *AIAA J.* **38** (1), 22–29.
- BATCHELOR, G.K. 1967 *An Introduction to Fluid Dynamics*. Cambridge University Press.
- BIRCH, J.M. & DICKINSON, M.H. 2001 Spanwise flow and the attachment of the leading-edge vortex on insect wings. *Nature* **412** (6848), 729–733.
- CALDERER, A., YANG, X., ANGELIDIS, D., KHOSRONEJAD, A., LE, T., KANG, S., GILMANOV, A., GE, L. & BORAZJANI, I. 2015 Virtual flow simulator. *Tech. Rep.* 004806MLTPL00. University of Minnesota.
- CHANG, C.-C. 1992 Potential flow and forces for incompressible viscous flow. *Proc. R. Soc. Lond. A: Math. Phys. Sci.* **437** (1901), 517–525.
- CHEN, L., CHENG, B. & WU, J. 2023a Vorticity dynamics and stability of the leading-edge vortex on revolving wings. *Phys. Fluids* **35** (9), 091301.
- CHEN, L., CHENG, C., ZHOU, C., ZHANG, Y. & WU, J. 2024 Flapping rotary wing: a novel low-Reynolds number layout merging bionic features into micro rotors. *Prog. Aerosp. Sci.* **146**, 100984.
- CHEN, L., WANG, L., ZHOU, C., WU, J. & CHENG, B. 2022 Effects of Reynolds number on leading-edge vortex formation dynamics and stability in revolving wings. *J. Fluid Mech.* **931**, A13.
- CHEN, L., ZHOU, C., WERNER, N.H., CHENG, B. & WU, J. 2023b Dual-stage radial–tangential vortex tilting reverses radial vorticity and contributes to leading-edge vortex stability on revolving wings. *J. Fluid Mech.* **963**, A29.
- CHEN, Y., GRAVISH, N., DESBIENS, A.L., MALKA, R. & WOOD, R.J. 2016 Experimental and computational studies of the aerodynamic performance of a flapping and passively rotating insect wing. *J. Fluid Mech.* **791**, 1–33.
- CLARK, C.J. 2021 Ways that animal wings produce sound. *Integr. Compar. Biol.* **61** (2), 696–709.
- COLONIUS, T. & LELE, S.K. 2004 Computational aeroacoustics: progress on nonlinear problems of sound generation. *Prog. Aerosp. Sci.* **40** (6), 345–416.
- COLONIUS, T., LELE, S.K. & MOIN, P. 1997 Sound generation in a mixing layer. *J. Fluid Mech.* **330**, 375–409.
- CURLE, N. 1955 The influence of solid boundaries upon aerodynamic sound. *Proc. R. Soc. Lond. A Math. Phys. Sci.* **231** (1187), 505–514.
- DAI, H., LUO, H. & DOYLE, J.F. 2012 Dynamic pitching of an elastic rectangular wing in hovering motion. *J. Fluid Mech.* **693**, 473–499.
- DEWEY, P.A., BOSCHITSCH, B.M., MOORED, K.W., STONE, H.A. & SMITS, A.J. 2013 Scaling laws for the thrust production of flexible pitching panels. *J. Fluid Mech.* **732**, 29–46.
- EHRENSTEIN, U. 2019 Thrust and drag scaling of a rigid low-aspect-ratio pitching plate. *J. Fluids Struct.* **87**, 39–57.
- ELDRIDGE, J.D. & JONES, A.R. 2019 Leading-edge vortices: mechanics and modeling. *Annu. Rev. Fluid Mech.* **51**, 75–104.
- ELLINGTON, C.P. 1984 The aerodynamics of hovering insect flight. III. Kinematics. *Phil. Trans. R. Soc. Lond. B Biol. Sci.* **305** (1122), 41–78.
- ELLINGTON, C.P., VAN DEN BERG, C., WILLMOTT, A.P. & THOMAS, A.L.R. 1996 Leading-edge vortices in insect flight. *Nature* **384** (6610), 626–630.
- FARASSAT, F. 2007 Derivation of formulations 1 and 1A of Farassat. *Tech. Rep.* NASA/TM-2007-214853. NASA Langley Research Center.
- FARHAT, C. & LAKSHMINARAYAN, V.K. 2014 An ALE formulation of embedded boundary methods for tracking boundary layers in turbulent fluid–structure interaction problems. *J. Comput. Phys.* **263**, 53–70.
- FFOWCS WILLIAMS, J.E. & HAWKINGS, D.L. 1969 Sound generation by turbulence and surfaces in arbitrary motion. *Phil. Trans. R. Soc. Lond. A Math. Phys. Sci.* **264** (1151), 321–342.
- FORD, C.W.P. & BABINSKY, H. 2013 Lift and the leading-edge vortex. *J. Fluid Mech.* **720**, 280–313.
- GARMANN, D.J. & VISBAL, M.R. 2014 Dynamics of revolving wings for various aspect ratios. *J. Fluid Mech.* **748**, 932–956.

## Evolution of vortices determines aeroacoustics of a wing

- GARMANN, D.J., VISBAL, M.R. & ORKWIS, P.D. 2013 Three-dimensional flow structure and aerodynamic loading on a revolving wing. *Phys. Fluids* **25** (3), 034101.
- GENG, B., XUE, Q., ZHENG, X., LIU, G., REN, Y. & DONG, H. 2017 The effect of wing flexibility on sound generation of flapping wings. *Bioinspir. Biomim.* **13** (1), 016010.
- GERMANO, M., PIOMELLI, U., MOIN, P. & CABOT, W.H. 1991 A dynamic subgrid-scale eddy viscosity model. *Phys. Fluids A: Fluid Dyn.* **3** (7), 1760–1765.
- GIBSON, G. & RUSSELL, I. 2006 Flying in tune: sexual recognition in mosquitoes. *Curr. Biol.* **16** (13), 1311–1316.
- GOLDSTEIN, D., HANDLER, R. & SIROVICH, L. 1993 Modeling a no-slip flow boundary with an external force field. *J. Comput. Phys.* **105** (2), 354–366.
- HAN, J.-S., CHANG, J.W., KIM, J.-K. & HAN, J.-H. 2015 Role of trailing-edge vortices on the hawkmothlike flapping wing. *J. Aircraft* **52** (4), 1256–1266.
- HARDIN, J.C. & POPE, D.S. 1994 An acoustic/viscous splitting technique for computational aeroacoustics. *Theor. Comput. Fluid Dyn.* **6** (5), 323–340.
- HIGHTOWER, B.J., WININGS, P.W.A., SCHOLTE, R., INGERSOLL, R., CHIN, D.D., NGUYEN, J., SHORR, D. & LENTINK, D. 2020 How hummingbirds hum: Oscillating aerodynamic forces explain timbre of the humming sound. [arXiv:2009.01933](https://arxiv.org/abs/2009.01933).
- HIRT, C.W., AMSDEN, A.A. & COOK, J.L. 1974 An arbitrary Lagrangian-Eulerian computing method for all flow speeds. *J. Comput. Phys.* **14** (3), 227–253.
- HOWE, M.S. 2003 *Theory of Vortex Sound*. Cambridge University Press.
- HUANG, Q., BHAT, S.S., YEO, E.C., YOUNG, J., LAI, J.C.S., TIAN, F.-B. & RAVI, S. 2023 Power synchronisations determine the hovering flight efficiency of passively pitching flapping wings. *J. Fluid Mech.* **974**, A41.
- HUANG, Q., LIU, Z., WANG, L., RAVI, S., YOUNG, J., LAI, J.C.S. & TIAN, F.-B. 2022 Streamline penetration, velocity error, and consequences of the feedback immersed boundary method. *Phys. Fluids* **34** (9), 097101.
- HUANG, W.-X. & TIAN, F.-B. 2019 Recent trends and progress in the immersed boundary method. *Proc. Inst. Mech. Engrs C: J. Mech. Engng Sci.* **233** (23–24), 7617–7636.
- HUANG, Y. & GREEN, M.A. 2015 Detection and tracking of vortex phenomena using Lagrangian coherent structures. *Exp. Fluids* **56** (7), 1–12.
- INADA, Y., AONO, H., LIU, H. & AOYAMA, T. 2009 Numerical analysis of sound generation of insect flapping wings. *Theor. Appl. Mech. Japan* **57**, 437–447.
- JARDIN, T. & DAVID, L. 2015 Coriolis effects enhance lift on revolving wings. *Phys. Rev. E* **91** (3), 031001.
- JEONG, J. & HUSSAIN, F. 1995 On the identification of a vortex. *J. Fluid Mech.* **285**, 69–94.
- JI, X., WANG, L., RAVI, S., TIAN, F.-B., YOUNG, J. & LAI, J.C.S. 2022 Influences of serrated trailing edge on the aerodynamic and aeroacoustic performance of a flapping wing during hovering flight. *Phys. Fluids* **34** (1), 011902.
- JI, X., WANG, L., RAVI, S., YOUNG, J., LAI, J.C.S. & TIAN, F.-B. 2024 Aerodynamic and aeroacoustic performance of a pitching foil with trailing edge serrations at a high Reynolds number. *Theor. Comput. Fluid Dyn.* **38**, 825–844.
- JONES, A.R. & BABINSKY, H. 2010 Unsteady lift generation on rotating wings at low Reynolds numbers. *J. Aircraft* **47** (3), 1013–1021.
- JONES, A.R. & BABINSKY, H. 2011 Reynolds number effects on leading edge vortex development on a waving wing. *Exp. Fluids* **51** (1), 197–210.
- JONES, A.R., MEDINA, A., SPOONER, H. & MULLENERS, K. 2016 Characterizing a burst leading-edge vortex on a rotating flat plate wing. *Exp. Fluids* **57** (4), 1–16.
- KANG, C.-K. & SHYY, W. 2013 Scaling law and enhancement of lift generation of an insect-size hovering flexible wing. *J. R. Soc. Interface* **10** (85), 20130361.
- KIM, D. & GHARIB, M. 2010 Experimental study of three-dimensional vortex structures in translating and rotating plates. *Exp. Fluids* **49**, 329–339.
- LAI, J.C.S. & PLATZER, M.F. 1999 Jet characteristics of a plunging airfoil. *AIAA J.* **37** (12), 1529–1537.
- LEE, J., CHOI, H. & KIM, H.-Y. 2015 A scaling law for the lift of hovering insects. *J. Fluid Mech.* **782**, 479–490.
- LELE, S. 1997 Computational aeroacoustics—a review. In *35th Aerospace Sciences Meeting and Exhibit*, p. 18. AIAA.
- LI, G.-J. & LU, X.-Y. 2012 Force and power of flapping plates in a fluid. *J. Fluid Mech.* **712**, 598–613.
- LIU, H., ELLINGTON, C.P., KAWACHI, K., VAN DEN BERG, C. & WILLMOTT, A.P. 1998 A computational fluid dynamic study of hawkmoth hovering. *J. Exp. Biol.* **201** (4), 461–477.

- LIU, K., LIU, X. & HUANG, H. 2022 Scaling the self-propulsive performance of pitching and heaving flexible plates. *J. Fluid Mech.* **936**, A9.
- LU, Y., SHEN, G.X. & LAI, G.J. 2006 Dual leading-edge vortices on flapping wings. *J. Exp. Biol.* **209** (24), 5005–5016.
- LYRINTZIS, A.S. 2003 Surface integral methods in computational aeroacoustics—from the (CFD) near-field to the (acoustic) far-field. *Intl J. Aeroacoust.* **2** (2), 95–128.
- MEDINA, A. & JONES, A.R. 2016 Leading-edge vortex burst on a low-aspect-ratio rotating flat plate. *Phys. Rev. Fluids* **1** (4), 044501.
- MENON, K., KUMAR, S. & MITTAL, R. 2022 Contribution of spanwise and cross-span vortices to the lift generation of low-aspect-ratio wings: insights from force partitioning. *Phys. Rev. Fluids* **7**, 114102.
- MITTAL, R. & IACCARINO, G. 2005 Immersed boundary methods. *Annu. Rev. Fluid Mech.* **37**, 239–261.
- NAGARAJAN, S., HAHN, S. & LELE, S. 2006 Prediction of sound generated by a pitching airfoil: a comparison of RANS and LES. In *12th AIAA/CEAS Aeroacoustics Conference (27th AIAA Aeroacoustics Conference)*, p. 2516. AIAA.
- NAGARAJAN, S. & LELE, S. 2005 Sound generation by unsteady airfoil motions: a study using direct computation and acoustic analogy. In *11th AIAA/CEAS Aeroacoustics Conference*, p. 2915. AIAA.
- NEDUNCHEZIAN, K., KANG, C.-K. & AONO, H. 2019 Effects of flapping wing kinematics on the aeroacoustics of hovering flight. *J. Sound Vib.* **442**, 366–383.
- PESKIN, C.S. 1972 Flow patterns around heart valves: a numerical method. *J. Comput. Phys.* **10** (2), 252–271.
- PESKIN, C.S. 2002 The immersed boundary method. *Acta Numerica* **11**, 479–517.
- PLATZER, M.F., JONES, K.D., YOUNG, J. & LAI, J.C.S. 2008 Flapping wing aerodynamics: progress and challenges. *AIAA J.* **46** (9), 2136–2149.
- POELMA, C., DICKSON, W.B. & DICKINSON, M.H. 2006 Time-resolved reconstruction of the full velocity field around a dynamically-scaled flapping wing. *Exp. Fluids* **41**, 213–225.
- RAVI, S., KOLOMENSKIY, D., ENGELS, T., SCHNEIDER, K., WANG, C., SESTERHENN, J. & LIU, H. 2016 Bumblebees minimize control challenges by combining active and passive modes in unsteady winds. *Sci. Rep.* **6** (1), 1–10.
- RINGUETTE, M.J., MILANO, M. & GHARIB, M. 2007 Role of the tip vortex in the force generation of low-aspect-ratio normal flat plates. *J. Fluid Mech.* **581**, 453–468.
- ROBERT, D. & GÖPFERT, M.C. 2002 Acoustic sensitivity of fly antennae. *J. Insect Physiol.* **48** (2), 189–196.
- SANDBERG, R.D., JONES, L.E., SANDHAM, N.D. & JOSEPH, P.F. 2009 Direct numerical simulations of tonal noise generated by laminar flow past airfoils. *J. Sound Vib.* **320** (4–5), 838–858.
- SANE, S.P. & DICKINSON, M.H. 2001 The control of flight force by a flapping wing: lift and drag production. *J. Exp. Biol.* **204** (15), 2607–2626.
- SEO, J.-H., HEDRICK, T.L. & MITTAL, R. 2019 Mechanism and scaling of wing tone generation in mosquitoes. *Bioinspir. Biomim.* **15** (1), 016008.
- SEO, J.-H., MENON, K. & MITTAL, R. 2022 A method for partitioning the sources of aerodynamic loading noise in vortex dominated flows. *Phys. Fluids* **34** (5), 053607.
- SHAHZAD, A., TIAN, F.-B., YOUNG, J. & LAI, J.C.S. 2016 Effects of wing shape, aspect ratio and deviation angle on aerodynamic performance of flapping wings in hover. *Phys. Fluids* **28** (11), 111901.
- SHAHZAD, A., TIAN, F.-B., YOUNG, J. & LAI, J.C.S. 2018 Effects of hawkmoth-like flexibility on the aerodynamic performance of flapping wings with different shapes and aspect ratios. *Phys. Fluids* **30** (9), 091902.
- SHYY, W., AONO, H., CHIMAKURTHI, S.K., TRIZILA, P., KANG, C.-K., CESNIK, C.E.S. & LIU, H. 2010 Recent progress in flapping wing aerodynamics and aeroelasticity. *Prog. Aerosp. Sci.* **46** (7), 284–327.
- SHYY, W., TRIZILA, P., KANG, C.-K. & AONO, H. 2009 Can tip vortices enhance lift of a flapping wing? *AIAA J.* **47** (2), 289–293.
- SINGER, B.A., BRENTNER, K.S., LOCKARD, D.P. & LILLEY, G.M. 2000 Simulation of acoustic scattering from a trailing edge. *J. Sound Vib.* **230** (3), 541–560.
- SPIETH, H.T. 1974 Courtship behavior in drosophila. *Annu. Rev. Entomol.* **19** (1), 385–405.
- SUEUR, J., TUCK, E.J. & ROBERT, D. 2005 Sound radiation around a flying fly. *J. Acoust. Soc. Am.* **118** (1), 530–538.
- TIAN, F.-B. 2020 Hydrodynamic effects of mucus on swimming performance of an undulatory foil by using the DSD/SST method. *Comput. Mech.* **65** (3), 751–761.
- TIAN, F.-B., LUO, H., SONG, J. & LU, X.-Y. 2013 Force production and asymmetric deformation of a flexible flapping wing in forward flight. *J. Fluids Struct.* **36**, 149–161.
- VISBAL, M.R. 2009 High-fidelity simulation of transitional flows past a plunging airfoil. *AIAA J.* **47** (11), 2685–2697.



*Evolution of vortices determines aeroacoustics of a wing*

- WANG, L. & TIAN, F.-B. 2019 Numerical study of flexible flapping wings with an immersed boundary method: fluid–structure–acoustics interaction. *J. Fluids Struct.* **90**, 396–409.
- WANG, L. & TIAN, F.-B. 2020 Numerical study of sound generation by three-dimensional flexible flapping wings during hovering flight. *J. Fluids Struct.* **99**, 103165.
- WANG, L., TIAN, F.-B. & LAI, J.C.S. 2020 An immersed boundary method for fluid–structure–acoustics interactions involving large deformations and complex geometries. *J. Fluids Struct.* **95**, 102993.
- WARREN, B., GIBSON, G. & RUSSELL, I.J. 2009 Sex recognition through midflight mating duets in culex mosquitoes is mediated by acoustic distortion. *Curr. Biol.* **19** (6), 485–491.
- WU, J., LIU, L. & LIU, T. 2018 Fundamental theories of aerodynamic force in viscous and compressible complex flows. *Prog. Aerosp. Sci.* **99**, 27–63.
- WU, J.C. 1981 Theory for aerodynamic force and moment in viscous flows. *AIAA J.* **19** (4), 432–441.
- WU, J.-Z., MA, H.-Y. & ZHOU, M.-D. 2007 *Vorticity and Vortex Dynamics*. Springer Science & Business Media.
- WU, J.-Z., PAN, Z.-L. & LU, X.-Y. 2005 Unsteady fluid-dynamic force solely in terms of control-surface integral. *Phys. Fluids* **17** (9), 098102.
- YOUNG, J. & GARRATT, M. 2020 Drones become even more insect-like. *Science* **368** (6491), 586–587.
- YOUNG, J. & LAI, J.C.S. 2007 Mechanisms influencing the efficiency of oscillating airfoil propulsion. *AIAA J.* **45** (7), 1695–1702.
- ZHOU, T., SUN, Y., FATTAH, R., ZHANG, X. & HUANG, X. 2019 An experimental study of trailing edge noise from a pitching airfoil. *J. Acoust. Soc. Am.* **145** (4), 2009–2021.